Interplay of valence states and magnetic interactions in the perovskite system LaNi$_{1-x}$Rh$_x$O$_3$

A. Slagtern Fjellvåg[a]*, Ø. Slagtern Fjellvåg[b], S. Kumar[a], A. Ruud[a,c] and A. Olafsen Sjåstad[a]*

[a]Centre for Materials Science and Nanotechnology, Department of Chemistry, University of Oslo, P.O. Box 1033, N–0315 Oslo, Norway

[b]Department for Neutron Materials Characterization, Institute for Energy Technology, PO Box 40, NO-2027, Kjeller, Norway

[c]Nordic Institute of Dental Materials, Sognsveien 70 A, Oslo 0855, Norway

*a.o.sjastad@kjemi.uio.no; a.s.fjellvag@smn.uio.no

Abstract

We report on the structural, magnetic and electronic properties of Rh substituted LaNiO$_3$, LaNi$_{1-x}$Rh$_x$O$_3$ ($0 \leq x \leq 1$). Increased Rh contents are associated with increased structural distortion, and we observe a phase transformation and an immiscibility gap between $0.15 \leq x \leq 0.25$, separating the *R–3c* and *Pnma* perovskite structure regimes. Structural evaluation by synchrotron X-ray diffraction, X-ray absorption spectroscopy and DC magnetic measurements suggest variations in oxidation state for the *B*-site cations, with Ni(II)/Rh(IV), in addition to Rh(III), dominating for high Rh-contents. Although ordering of Ni(II)/Rh(IV) is possible, no *B*-site ordering between Ni and Rh is observed for any composition. A metal-to-insulator transition occurs upon Rh-substitution, correlating with the structural transition. DC- and AC magnetic measurements reveal that several of the compositions are magnetically frustrated with both antiferro- and ferromagnetic behaviour at low temperatures. The antiferromagnetic interactions are dominating, while the ferromagnetic interactions increase with increasing Rh-content, to a maximum at $x = 0.80$ and $x = 0.90$ in LaNi$_{1-x}$Rh$_x$O$_3$. The mixed valence states are assumed to contribute with a ferromagnetic super-exchange interaction between Ni(II) and Rh(IV).

1. Introduction

Materials displaying correlated electron behaviour has received an increasing amount of attention over the last decades due to the multitude of exotic phenomena in such systems. An important example is the simple perovskite LaNiO$_3$ and related derivatives [1-8], which are continuously under investigation after the discovery of the first superconducting nickelate Sr$_{0.2}$Nd$_{0.8}$NiO$_2$ [9]. Upon *B*-site substitution, *B*-site ordering may also occur, creating an entire new family of materials [10]. Internal variations in ordering phenomena is also possible, such as in Sr$_2$FeMoO$_6$, where the grain structure and degree of short range and long range Fe-Mo ordering is closely related to variations in magnetoresistance and the ferromagnetic strength [11, 12].

In investigations of LaNiO$_3$, total scattering analysis has been used to probe the short range ordering, which reveal that LaNiO$_3$ may be at the borderline of insulating behaviour due to Jahn-Teller distortions of the $e_g{}^1$ electron configuration of Ni(III), which would force localization [1]. For long, LaNiO$_3$ was expected to be a weak ferromagnet due to the itinerancy $e_g{}^1$ electron [8]. However, recent investigations of LaNiO$_3$ single crystals display an antiferromagnetic-like transition around 150-160 K [13, 14], causing uncertainty of the true magnetic ground state of LaNiO$_3$. Modifications of the electronic properties of LaNiO$_3$ may further be promoted through *A*- or *B*-site substitution, giving rise to metal-insulator transitions (MIT) [3, 6, 15-19] or magnetic transitions [20-24]. In general, the MIT is caused

by a reduction (sharpening) of the Ni-O-Ni bond angle by *A*-site (or *B*-site) substitution, or reduction of the electron population of the Ni e_g-orbitals from *B*-site substitution. On the other hand, the magnetic properties emerging from *B*-site substitution may seem unpredictable, such as in the system $LaNi_{1-x}Co_xO_3$, where changes in oxidation- and spin states lead to modifications in the magnetic properties [21, 25]. In this way, non-stoichiometric compositions may give new and unexpected electronic properties.

The ferromagnetic interaction between Ni(II) and Rh(IV), first predicted by Goodenough [26], then investigated by Battle and Vente [24], and Schinzer [23], has attracted our attention. They focused on the stoichiometric compound, $LaNi_{0.50}Rh_{0.50}O_3$, searching for ferromagnetic super-exchange interactions between Ni(II) and Rh(IV). However, the compound was found to contain only Ni(III) and Rh(III), showing spin glass behaviour at low temperatures, and insulting properties over a wide temperature range [27]. In the current study, we investigate the entire system $LaNi_{1-x}Rh_xO_3$, aiming to obtain deeper insight into the oxidation states of Ni and Rh through this system, and correlate this to magnetic interactions. Because Rh and Co have the same *d*-electron configuration, and the +IV oxidation state is more easily stabilized for Rh, a comparison with Co-substituted $LaNiO_3$ is very interesting. Here, we demonstrate the effect of a wet chemical synthesis route to produce phase pure samples in the perovskite system $LaNi_{1-x}Rh_xO_3$. We pay special attention to the crystal structure and oxidation states of Ni/Rh through synchrotron radiation X-ray diffraction (SR-XRD) and X-ray absorption spectroscopy (SR-XAS), as variations in structure and oxidation state is expected to influence both magnetic and conduction properties. Additionally, the known metallic properties of Sr_2RhO_4 [28, 29] and the high pressure phase $SrRhO_3$ [30] leads us to ask how Rh-substitution and possible redox reactions with Ni may affect the metallic properties in this system compared to other $LaNi_{1-x}M_xO_3$ systems, where *M* = 3*d*-element.

2. Experimental

Nitrate salts of the relevant elements, $La(NO_3)_3 \times 6\ H_2O$ (99.9 %; Alfa), $Ni(NO_3)_2 \times 6H_2O$ (99 %; KEBO Lab) and $Rh(NO_3)_3 \times H_2O$ (99.9 %; Sigma-Aldrich) were dissolved in water and their molar concentrations (mol / g) were determined by thermogravimetric analysis. $Mg(CH_3COO)_2 \times 4H_2O$ (99.5 %; Fluka) were used as received. All $LaRh_{1-x}Ni_xO_3$ samples and La_2MgRhO_6 (reference sample for SR-XAS) were synthesized following a citric acid complexation method. Stoichiometric amounts of nitrate solutions were weighed out for each element (La, Ni, Rh) and $Mg(CH_3COO)_2 \times 4H_2O$), and 50 g of citric acid monohydrate ($C_6O_7H_8 \cdot H_2O$, 99 %, Sigma-Aldrich) was added per gram of oxide product. The solution was boiled until complete removal of water and nitrous gasses, followed by overnight heat treatment at 180 °C in a heating cabinet. The obtained crust was crushed and calcined at 400 °C for 12 hours in static air, before pelletizing and sequential high temperature heat treatment at 850 °C and 1000 °C, both for 12 hours in 1 atm of dynamic O_2 (from AGA, 5.0 purity). For $LaNiO_3$ the high temperature heat treatment was performed twice at 850 °C in 1 atm O_2 (from AGA, 5.0 quality) for 48 hours. Samples were annealed in pure O_2 in order to produce samples with stoichiometric oxygen content.

Structural characterization by synchrotron X-ray diffraction (SR-XRD) and synchrotron X-ray absorption spectroscopy (XAS) was performed at beamline BM01B at the Swiss-Norwegian Beam Lines (SNBL), European Synchrotron Radiation Facility (ESRF), Grenoble France [31]. SR-XRD experiments were performed using a 2D Dexela detector with wavelength $\lambda = 0.50506$ Å. Rietveld refinements were performed using the software TOPAS V5 [32] on data sets with ~3630 data points, *Q*-range from 1.3 to 11.48 Å^{-1}, and 254 (*R-3c*) and 832 (*Pnma*) *hkl* indices. The refinements were performed with basis in structures reported by Kojima *et al.* [33] and Battle and Vente [24]. The

Thompson-Cox-Hasting pseudo Voigt function was used to describe the peak shape for all samples, and the zero error, scale factor, unit cell parameters, atomic positions and Debye-Waller factors were refined. Refinements with negative Debye-Waller factors were excluded, and crystallite size was not included in the models. SR-XAS data for the Rh K-edge were measured in transmission mode using a Si(111) channel-cut monochromator with a second detuned crystal to reduce higher harmonics. The ATHENA software was used in SR-XAS data analysis for spectrum normalization to an edge jump of unity [34], with all scans calibrated to the theoretical Rh K-edge at 23220 eV based on Rh metal foil. Oxidation state reference materials for Rh(III) and Rh(IV) are $LaRhO_3$ and La_2MgRhO_6, respectively. La_2MgRhO_6, which was solely used as a reference for Rh(IV), was found by means of XRD to contain minute quantities of La_2O_3 (< 1 mol %).

Magnetic and electronic transport measurements were performed using a Quantum Design physical properties measurement system (QD-PPMS). Temperature dependent DC magnetization measurements were performed from 4 to 300 K using a 2 kOe persistent external DC-field, and field dependent DC magnetization measurements were performed at 4 K with a DC field variating between ± 90 kOe. Temperature dependent AC magnetization data were collected from 4 to 45 K with and without a 2 kOe persistent external DC field, and with a 10 Oe AC field with frequencies of 177, 1117 and 9917 Hz, respectively. For resistivity measurements, regular pellets annealed at 1000 °C in O_2 (850 °C in O_2 for $LaNiO_3$) was used, with silver paste electrodes coated on the sample and gold wires between the sample and the transport puck. The applied electrical current for the measurements of the individual samples was selected to achieve a linear IV-curve with zero crossing before starting the measurement.

3. Results and Discussion

3.1 Structural aspects

Initial attempts using a solid state synthesis route on selected compositions in the system $LaNi_{1-x}Rh_xO_3$ yielded samples with significant Rh_2O_3-impurities. To obtain homogeneous and phase pure samples, we therefore turned to a wet chemical synthesis route. According to SR-XRD, all $LaNi_{1-x}Rh_xO_3$ ($0 \leq x \leq 1$) samples prepared by a wet-chemical synthesis route are phase pure, except $LaRhO_3$ ($x = 1$), which contains < 1 mol% of Rh_2O_3.

The two end members in the system, $LaNiO_3$ and $LaRhO_3$, are reported to adopt distorted perovskite type structures with different symmetries; *R-3c* and *Pnma*, respectively [8, 35]. Through analysis of the SR-XRD patterns, we find that the $LaNi_{1-x}Rh_xO_3$ series obtain these two space groups for the entire compositional range. When substituting Rh for Ni in $LaNiO_3$, the large size of Rh causes an increased tilt of the octahedra, reducing the symmetry to orthorhombic. The characteristic low angle (011)-peak for the orthorhombic phase (*Pnma*) is absent in the diffraction patterns (Figure S1), indicating the absence of *B*-site ordering for all compositions [23, 24]. Furthermore, an immiscibility gap is observed in the compositional interval $0.10 < x < 0.30$, see Figure 1a. For the compositions $0.15 \leq x \leq 0.25$, the two phases co-exist (space group *R-3c* and *Pnma*), with an observed volume increase through the phase transformation (shaded area, Figure 1a). We observe an increase of the pseudocubic unit cell volume with increasing Rh content (Figure 1a) on both sides of the immiscibility gap, consistent with a larger average ionic radii when Rh is substituted for Ni. Rh-substitution also causes an increase in *M*-O bond distances and a reduction of the *M*-O-*M* bond angles, which deviate increasingly from 180° (Table S1). This correlates with increased structural distortions, in line with the decrease in tolerance factor (Table S1).

In the structural analysis, a volume increase is found for the orthorhombic (*Pnma*) samples ($x = 0.15 - 0.25$) inside the structural two-phase region (Figure 1a). However, we believe this to be an artefact (Figure 1a). The Rietveld refinement (Figure S1) may be easily influenced by the fact that the pseudocubic cell parameters are very similar for most compositions ($b \approx \sqrt{2}a \approx \sqrt{2}c$). Through the entire system, the a and b cell parameters increase, while the change in the c-axis is small. Additionally, around $x = 0.40$ the a- and c-axis are equally large, before the c-axis contracts, see Figure 1b. This may originate from the large anisotropy of the orthorhombic $b^+a^-a^-$ tilt-deformation of the perovskite structure [36], and is similar to observations reported by Li *et al.* [37] for $LaCo_{1-x}Rh_xO_3$. The MO_6-octahedra are slightly asymmetric in terms of bond lengths (Table S1), but compared to the heavily Jahn-Teller distorted compound $LaMnO_3$, the bond length asymmetry is small. At most, we observe a M-O bond length difference of 0.12 Å for the $x = 0.50$ composition, while in $LaMnO_3$ the largest Mn-O bond length difference is 0.28 Å [38].

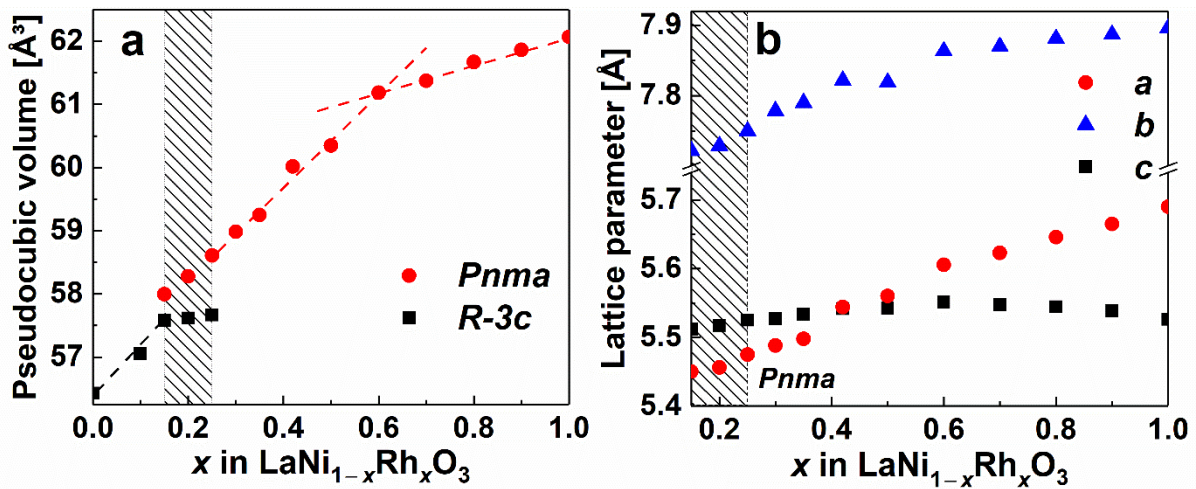**Figure 1. (a) Pseudocubic unit cell volume of $LaNi_{1-x}Rh_xO_3$ as a function of x ($0 \leq x \leq 1$). The dashed lines indicate areas with a linear increase in the pseudocubic unit cell volume. (b) Unit cell parameters for orthorhombic (*Pnma*) $LaNi_{1-x}Rh_xO_3$ versus x ($0.15 \leq x \leq 1$). The hatched area indicates the two-phase region. The lattice parameters for the rhombohedral (*R-3c*) samples can be found in Figure S2.**

Notably, the pseudocubic unit cell volume (Figure 1a) of the orthorhombic samples (*Pnma*) shows a deviation from Vegard's law [39], with a distinct change in the slope at $x \approx 0.60$. Such a deviation may come from mixed oxidation states through the perovskite system, causing different ionic sizes to dominate the different compositions. Using reported ionic radii (radius: Ni(III)/Rh(III) = 0.56/0.67 Å; Ni(II)/Rh(IV) = 0.67/0.60 [40]), the theoretical unit cell volume is evaluated in the two scenarios; Ni(III)/Rh(III) and Ni(II)/Rh(IV) (Figure S3a). In the case of the Ni(III)−Rh(III) solid solution, a linear increase in unit cell volume is expected with increasing substitution level of Rh, following Vegard's law. In the case of Ni(II)−Rh(IV), we expect a larger unit cell volume throughout the solid solution ($LaNi_{1-x}Rh_xO_3$), but with a distinct shift in the slope of the pseudocubic unit cell volume for $x = 0.50$ (Figure S3a). The experimental unit cell volume lies between the two models, indicating a mixed situation between the two models. Thus, analysis of the crystal structure suggests mixed oxidation states with both Ni(III)/Rh(III) and Ni(II)/Rh(IV) present.

Relative to Vegard's law, the experimental volume shows a maximum deviation at $x \approx 0.60$ (Figure 1a), which is close to the theoretical maximum deviation at $x = 0.50$ (Figure S3a)). We can estimate the relative amount of the Ni(II)/Rh(IV) pair by comparing the theoretical models and experimental volume (Figure S3b). For samples with high Rh-content ($x \geq 0.6$), ~60 % of the Ni exist as Ni(II), and a

corresponding amount of Rh is oxidized to Rh(IV). Mixed oxidation states with mainly Ni(II)–Rh(IV) is therefore in compliance with the experimental data. The fact that we do not have any indication of a complete charge division from Ni(III)/Rh(III) into Ni(II)/Rh(IV) may explain why no *B*-site ordering is observed (Figure S1), in compliance with reports by Vasala and Karppinen [10].

The likely presence of Ni(II)/Rh(IV) species in the solid solution is further corroborated by SR-XAS, Figure 2. We have compared the Rh K-edge for $LaNi_{1-x}Rh_xO_3$ ($0.58 \leq x \leq 1.00$) with reference samples (Rh(III): $LaRhO_3$, Rh(IV): La_2MgRhO_6). With increasing Ni content, we clearly observe a shift in the K-edge of Rh from the Rh(III) reference edge towards the Rh(IV) reference edge, see black arrow in Figure 2. We also observe that the two main absorption peaks at 23226 and 23237 eV for the $LaNi_{1-x}Rh_xO_3$ samples shifts in line with the Rh(III)- and Rh(IV) references. These observations support the presence of the Ni(II)/Rh(IV) configuration, and agree with our unit cell volume considerations above. In addition, our findings corroborates well with reports by Shibasaki *et al.* [41] and Smith *et al.* [27] on the Ni(II)/Rh(IV) couple in $LaNi_{1-x}Rh_xO_3$ and our DC-magnetization measurements presented below.

The solid solution $LaNi_{1-x}Rh_xO_3$ hence shows a significant degree of charge division into Ni(II) and Rh(IV), however, without any sign of Ni and Rh to adopt different sites in the crystal structure. Similarities can be drawn to the order-disorder phenomena in Sr_2FeMoO_6 [11], where short-range ordering between Fe and Mo is always present, regardless of the long-range order achieved by heat treatments. The charge division into Ni(II) and Rh(IV) could therefore be an indication of short-range ordering between Ni and Rh in the $LaNi_{1-x}Rh_xO_3$ system.
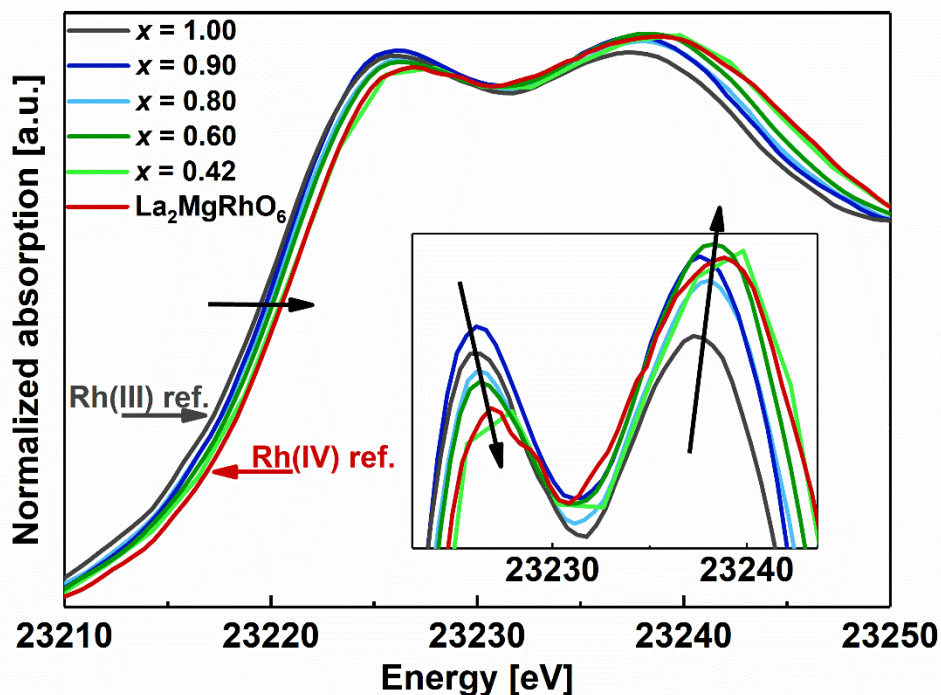

Figure 2. SR-XAS data of the Rh K-edge for selected samples in the $LaNi_{1-x}Rh_xO_3$ series ($0.42 \leq x \leq 1.00$). $LaRhO_3$ (dark grey) acts as a Rh(III) reference and La_2MgRhO_6 (dark red) acts as Rh(IV) reference. The black arrows indicate the changes in the absorption spectrums from the Rh(III) reference and towards the Rh(IV) reference with increasing amounts of Ni in $LaNi_{1-x}Rh_xO_3$.

3.2 Electronic transport properties

LaNiO$_3$ and LaNi$_{0.90}$Rh$_{0.10}$O$_3$ both display metallic conductivity, while compositions with $x \geq 0.30$ display semiconducting/insulating behaviour, see Figure 3. Of the two metallic compounds, the resistivity of LaNi$_{0.90}$Rh$_{0.10}$O$_3$ is one order of magnitude higher than that of LaNiO$_3$. The Fermi-liquid behaviour of LaNiO$_3$ (Figure S3, Table S2) [8] is absent in LaNi$_{0.90}$Rh$_{0.10}$O$_3$, as the latter becomes significantly less metallic compared to LaNiO$_3$ due to the increased disorder introduced by the 10 % B-site Rh-substitution (Figure S4). This is evident from the T^3-temperature dependency of the resistivity [42] in the temperature range 28 - 12 K, followed by an increase in resistivity below 10 K (Figure S5). We interpret the increase in resistivity as weak electron localization due to the B-site disorder in the compound, a common feature for materials close to a metal-insulator transition due to substitution [6, 43]. However, this does not necessarily mean that the material becomes insulating below 10 K. More detailed low temperature ($T < 1$ K) resistivity experiments are recommended to evaluate this fully. At elevated temperature ($T > 50$ K), however, the two compounds behave similarly, and electron-phonon interactions dominate the resistivity for both compounds; see the results from the temperature dependent analysis presented in Figure S4-S5 and Table S2.

For LaNi$_{1-x}$Rh$_x$O$_3$ samples with $x \geq 0.30$, the semiconducting/insulating behaviour is observed in the entire analysed temperature region, with resistivity values slightly higher, but similar, to previous reports [27, 41]. A compositional driven MIT therefore occurs somewhere in the interval $0.10 < x < 0.30$, correlating with the structural phase transformation where LaNi$_{1-x}$Rh$_x$O$_3$ transform from R-$3c$ to $Pnma$ (described above). The MIT is therefore likely caused by the increased structural deformations induced by substituting Ni with the significantly larger Rh-atom. This causes the M-O-M bond angle to be reduced beyond the necessary angle to maintain a metallic interaction ($\theta > \sim156°$ [3]) between the Ni e_g and O $2p_\sigma$ orbitals. A similar effect due to B-site substitution is reported in several other LaNi$_{1-x}$$M_xO_3$ systems (M = Co, Fe, Mn) [18, 44, 45], and furthermore as a temperature dependent transition in RENiO$_3$ (RE = La–Dy) [3, 15, 17], where increased distortions (low t-factor) result in a higher transition temperature for the MIT. The effect of structural deformations is evident from the MIT in LaNi$_{1-x}$Co$_x$O$_3$. Here, the structure is not further distorted by B-site substitution and remain rhombohedral (R-$3c$) for all x, allowing high Co-substitutions before the MIT occurs ($x_{MIT} \approx 0.65$ [6]). This stands in contrasts to Rh-substitution, where much lower substitutions cause the MIT ($0.10 < x_{MIT} < 0.30$). One can furthermore speculate on the fact that Rh(IV) is known to cause metallic properties in some oxides (SrRhO$_3$ [30], Sr$_2$RhO$_4$ [29]), and if this should impact in the LaNi$_{1-x}$Rh$_x$O$_3$ system, where significant amounts of Rh(IV) is present (Figure 2). With detailed analysis, we observe that the sample with $x = 0.30$ is at the border of being metallic at elevated temperatures (Figure S6), making it almost possible to fit resistivity data using a power law, such as for metals [6]. However, we believe that $x = 0.30$ remains insulating, and we conclude that the structural impact of the large Rh-atom exceeds the gain from Rh(IV) on the metallicity in this substitutional series.

For all insulating compositions ($x \geq 0.30$) we analyse the temperature dependence of the resistivity at elevated temperature ($T > 80\,K$) using the Arrhenius model for $x \leq 0.80$ and the Polaron model [46, 47] for $x \geq 0.90$, based on what provides the best fit (Figure S7-S8). We find that both the magnitude of the resistivity and the activation energy increases with increasing Rh-content (x), as expected from the non-conducting nature of Rh(III) (Figure S9, Table S3). However, for $x = 0.90$ and $x = 1.00$ the activation energy is significantly lowered due to the formation of polarons (Figure S9), which aid in the conduction of the electrons. We find that $x = 0.90$ contains large polarons with a low effective mass and that $x = 1.00$ contains small polarons with a high effective mass (see calculations in Supplemental).

It is still important to remember that even though the activation energy for electron hopping is reduced for these two compositions, it is mainly the temperature dependence of the resistivity which is changed, as the overall value of the resistivity depend on several factors. The cause of polaron formation in samples with $x \geq 0.90$, but not in samples with $x \leq 0.80$, is not known. But the low activation energy for $x = 0.90$ compared to $x = 1.00$ is most probably caused by the larger amount of charge carriers in $x = 0.90$, due to the valence state interplay between Ni and Rh, which is not present in $x = 1.00$.

Moving on to lower temperatures ($T < \sim 80$ K), where electron-electron interactions dominate, we find that different theories of variable range hopping (VRH) conduction [46, 48-50] fits well with the LaNi$_{1-x}$Rh$_x$O$_3$ system for all insulating samples ($0.30 \leq x \leq 1.00$) (Figure S10, Table S3). In VRH conduction, the localized charge carriers hop from one to another localized state near the Fermi level. Here, the subtle interplay between the lowest energy differences and shortest hopping distance defines where the localized charge carrier will hop. Therefore, it may hop different distances, depending on which atom that contains the lowest energy state nearby. In the LaNi$_{1-x}$Rh$_x$O$_3$ system, we find that 3-dimensional Mott VRH ($\log \rho \propto T^{-\frac{1}{4}}$) [48] fits best for $x = 0.30$, that 2-dimensional (2D) Mott VRH ($\log \rho \propto T^{-\frac{1}{3}}$) [48] fits best for $x = 0.40$ and $x = 0.50$, and that the 2D Efros-Shklovskii VRH ($\log \rho \propto T^{-\frac{1}{2}}$) [50] fits best for $x = 0.60-1.00$. This implies that that there is a compositional driven change in conduction mechanism through the system, and that it changes towards preferring 2D hopping for $x \geq 0.40$. However, the structure is described as a perovskite with a 3D network of corner-connected octahedra, where the only structural feature which could explain such 2D hopping is the highly anisotropic M-O bond distances and the low t-factor (Table S1). The electron may therefore, on a local scale, see the most desirable hopping locations nearby in a 2D plane. Additionally, this feature may also be correlated to the change in valence states through the system, and the change in magnetic interactions upon Rh-substitution (see section below). We recommend further investigations of the observed conduction phenomena at both high and low temperature, with focus on correlations with valence states and magnetic interactions.
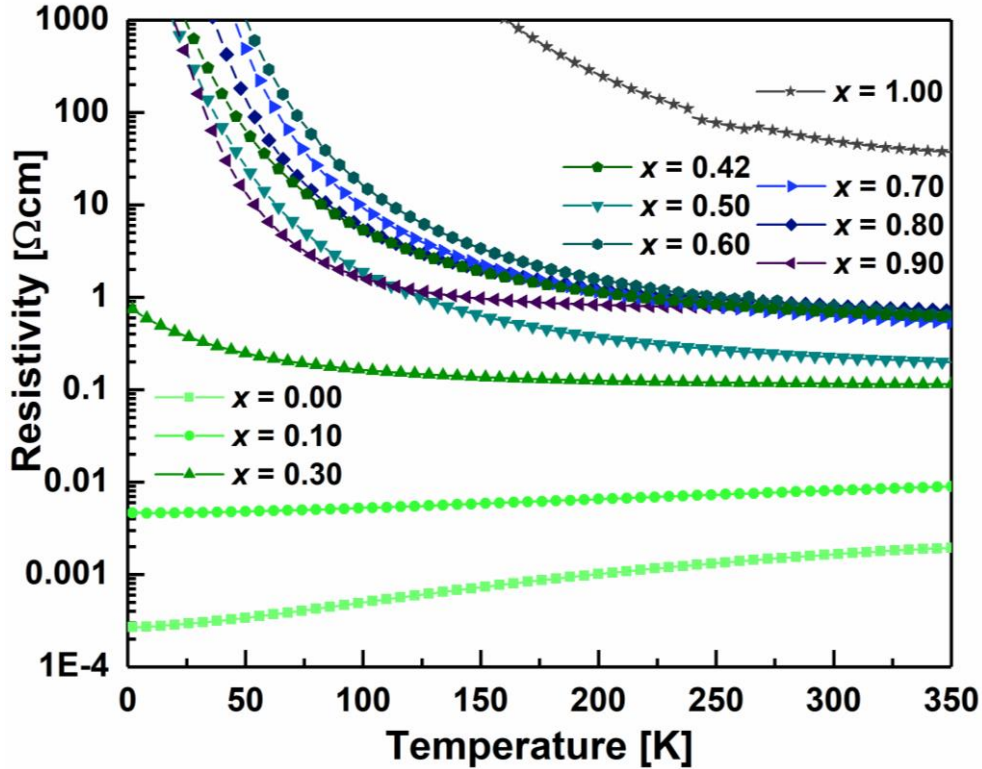
Figure 3. Measured resistivity of LaNi$_{1-x}$Rh$_x$O$_3$ ($0 \leq x \leq 1.00$) versus temperature. Sample compositions are given in the figure.

3.3 Magnetic measurements

3.3.1 High temperature region (paramagnetic region)

We find LaNiO$_3$ and LaRhO$_3$ to be Pauli paramagnetic and diamagnetic, respectively (Figure S10), in agreement with previous work on powder samples [8, 41]. For the intermediate compositions in LaNi$_{1-x}$Rh$_x$O$_3$, paramagnetic behaviour is observed above $\sim$30 K (Figure S11), also for the weakly metallic sample with $x = 0.10$. By using the Curie-Weiss relation, we find a linear $1/\chi$ temperature dependency above $\sim$150 K for compositions with $0.10 \leq x \leq 0.90$. However, the metallic conductivity for $x = 0.10$ makes the results inconclusive for this sample. For the compositions crystallizing with orthorhombic symmetry ($x \geq 0.30$) the experimental magnetic moments are compared to theoretical magnetic moments calculated using a Russel-Saunders coupling scheme (Figure S12 and Table S4) [51]. The experimental paramagnetic moments are higher than those expected when fixing the oxidation states to Ni(III) and Rh(III). The difference between observed and calculated magnetic moments can be explained by the presence of significant contributions of Ni(II) and Rh(IV), in compliance with structural considerations and SR-XAS. Further, it cannot be ruled out if spin orbit coupling of Rh(IV) gives a small additional contribution to the magnetic moment (Figure S12).

The Curie-Weiss analysis further provides θ_{CW}-values, and thereby indicate the type of dominating magnetic interactions for each composition. At high Ni-content, θ_{CW} is large and negative, while for increasing Rh-content, θ_{CW} becomes much less negative, but still remaining negative (Table S4). This indicates strong antiferromagnetic short-range interactions for the Ni-rich compositions, which decrease significantly in strength with increasing Rh-content.

3.3.2 Low temperature magnetic measurement

For several compositions in the $LaNi_{1-x}Rh_xO_3$ series, a small difference is observed between the field- and zero-field cooled DC-magnetization curves below $10 - 20$ K (Figure S11). This has previously been suggested to be caused by a spin-glass transition at $T_g \approx 10$ K for $LaNi_{0.50}Rh_{0.50}O_3$ [23, 24]. To characterize the low temperature state, field dependent magnetic measurements were performed at 4 K, see Figure 4. An interesting trend appears when considering the field dependent magnetization for the different compositions. For $x \leq 0.50$, a linear magnetization with no hysteresis is observed, like the behaviour of para- or antiferromagnetic materials. However, for $0.60 \leq x \leq 0.80$, the magnetization signal increases significantly and obtains a S-like shape versus applied magnetic field. The samples show a small hysteresis when reversing the magnetic field, and the M(H) magnetization show tendencies towards saturation, although not complete. For $x = 0.90$ the magnetization is reduced, but with a strong tendency towards saturation. Finally, for $x = 1.00$ the sample turns completely diamagnetic.

Among all the samples in the compositional series $LaNi_{1-x}Rh_xO_3$, the saturation magnetization is highest for $x = 0.80$. The magnetization at 90 kOe for $x = 0.80$ is ~ 0.15 μ_B/f.u., which is one quarter of the maximum magnetization assuming pure ferromagnetic ordering in $LaNi(II)_{0.20}Rh(III)_{0.60}Rh(IV)_{0.20}O_3$, when assuming complete charge division from Ni(III)/Rh(III) into Ni(II)/Rh(IV). Considering the $x = 0.90$ sample, the magnetization of ~ 0.09 μ_B/f.u. is approximately one third of the maximum magnetization, assuming pure ferromagnetic ordering in $LaNi(II)_{0.10}Rh(III)_{0.80}Rh(IV)_{0.10}O_3$. Furthermore, by dividing the M(H)-magnetization on the amount of available Ni(II)-Rh(IV) pairs from the stoichiometry of the structure, *i.e.* 0.2 for $x = 0.90$ and 0.4 for $x = 0.80$, the relative saturation magnetization becomes highest for $x = 0.90$ (inset in Figure 4). This indicates the existence of ferromagnetic properties for $0.60 \leq x \leq 0.90$, which increases with increasing Rh-content, and is strongest for $x = 0.90$.

To further investigate the low temperature phenomena, AC-magnetization measurements were performed for $x = 0.42$, 0.50, 0.70 and 0.80, see Figure 5. For $x = 0.50$, a weak transition occurs at 30 K, which can be easily suppressed by a 2 kOe DC-field, the same field as used in DC-magnetic measurements (Figure S14). Furthermore, for all four samples, a transition occurs at $T_m \approx 10$ K, which show intensities both for the real and imaginary component of the susceptibility, indicating a transition from a paramagnetic to a ferro-/ferrimagnetic state [52]. Notably, the transition temperatures do not change with frequency, and only a small increase in intensity for lower frequencies is observed. Compared to other reported spin-glass systems, the observed frequency dependence is low [53], ruling out the likeliness of a spin-glass transition. We therefore believe that the magnetic transition at $T_m \approx 10$ K is not a spin glass transition, but a transition from paramagnetic to a mixed ferro-/antiferromagnetic state, which depend on short range interactions and local structural ordering inside the compound.

Considering the intensity of the AC- and DC-magnetization measurements (Figure 5, Figure S11), the saturation magnetization in the field dependent measurement (Figure 4, Figure S13) and the θ_{CW} values (Table S4), we see that they all increase with increasing Rh-content. This indicates a trend of increased ferromagnetic interactions with increasing Rh-content. Considering the rules from Goodenough [26], which expects a moderate ferromagnetic super-exchange interaction between Ni(II) and Rh(IV), the increased ferromagnetism for increasing Rh-contents may be explained by the corresponding shift in valence states from Ni(III)/Rh(III) to Ni(II)/Rh(IV), as discussed above. We therefore believe that the magnetic transition at $T_m \approx 10$ K is into a mixed ferro-/antiferromagnetic state, with competing magnetic interactions depending on valence states. In this scenario, Ni(III)/Rh(III) will favour antiferromagnetism, while Ni(II)/Rh(IV) may favour ferromagnetic interactions. However, due to the

random distribution of Ni and Rh in the structure, it is highly difficult to imagine how a ferro- or antiferromagnetic ordering would look like in the structure. The local structure may therefore dictate the magnetic ordering.

It is also possible that the compounds adopt a ferrimagnetic state, due to the mixture in oxidation states and several possible magnetic interactions. This may also cause increased magnetization with increased Rh-content, and it is beyond the scope of this investigation to understand the true magnetic interactions in the compounds. If the Ni(II) and Rh(IV) sub-lattice was ordered, the magnetic interactions could have been much stronger than in the present case, and the origin behind the observed trend in magnetization could be resolved. With the current results, we believe an ordered Ni(II)/Rh(IV) compound could be the path to a new ferromagnetic compound, and provide insight into the magnetic interactions of Ni(II) and Rh(IV).
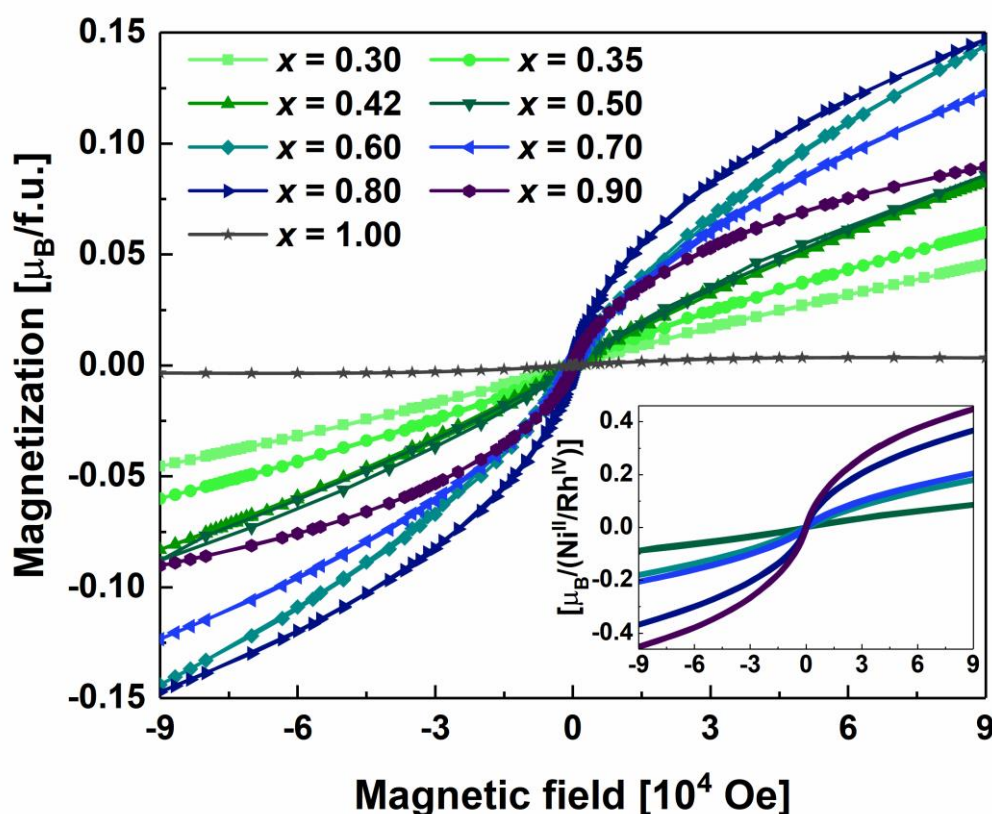

Figure 4. Field dependent magnetization measurements of selected members (x = 0.30, 0.35, 0.42, 0.50, 0.60, 0.70, 0.80, 0.90, 1.00) in the LaNi$_{1-x}$Rh$_x$O$_3$ series at T = 4 K between ± 90 kOe. The sample compositions are indicated in the figure by its x value. The intensity unit is in Bohr magnetons per formula unit (μ_B/f.u.). The inset shows the field dependent magnetization measurement where the intensity is divided by the amount of available Ni(II)/Rh(IV) pairs, i.e. 0.2 for x = 0.90 and 0.4 for x = 0.80.
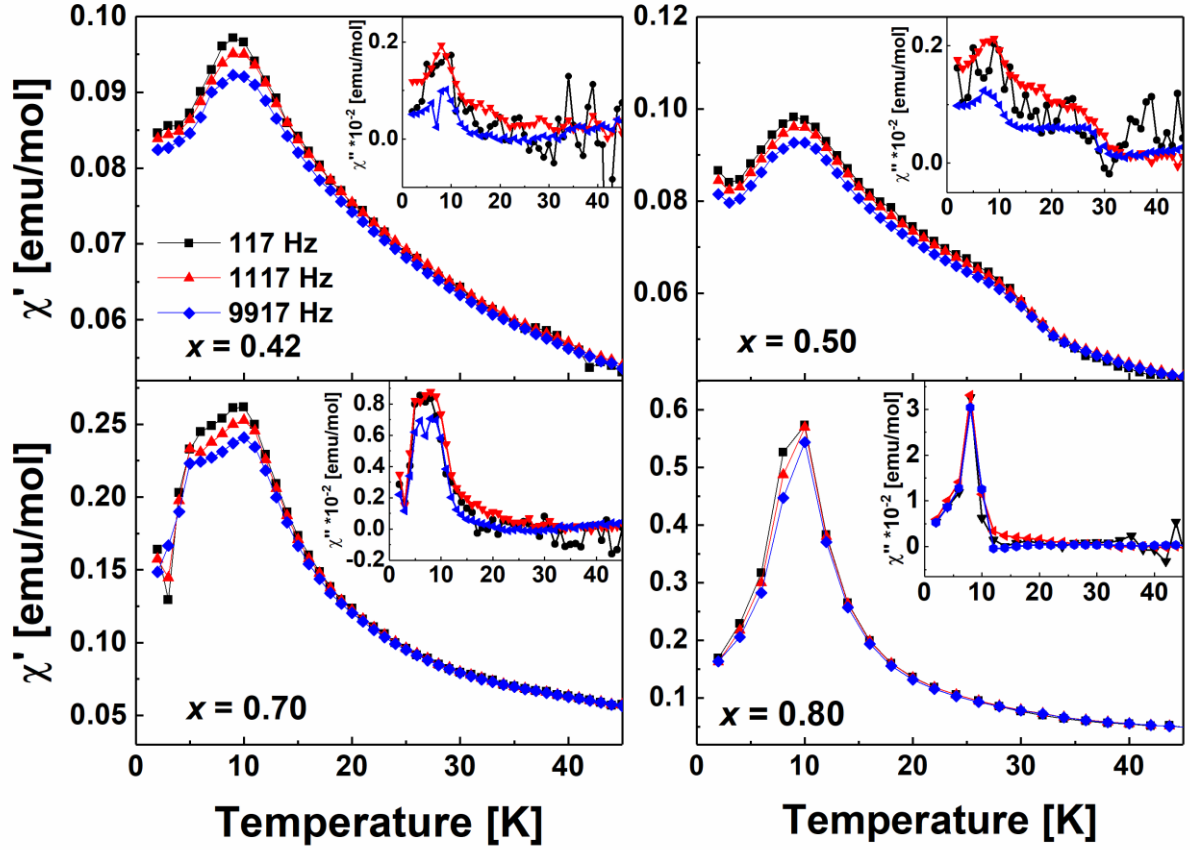
Figure 5. AC-susceptibility from 2 to 45 K using a 10 Oe and 117, 1117 and 9917 Hz AC-field for four different compositions in the LaNi$_{1-x}$Rh$_x$O$_3$ series, with the x-value written in the figure. The real component of the susceptibility (χ') is shown in the main graph, and the imaginary component (χ'') is shown in the inset.

4. Conclusion

We have demonstrated that a wet chemical synthesis route can be used to successfully synthesize all compositions in the perovskite system LaNi$_{1-x}$Rh$_x$O$_3$ ($0 \leq x \leq 1$). Our main findings of the structure-property relations of the LaNi$_{1-x}$Rh$_x$O$_3$ system are summarized in Figure 6. Through the system, a structural phase transformation from *R-3c* to *Pnma* occurs due to the large size of the substituent Rh-atom, with an immiscibility gap for $0.15 < x < 0.25$. Rh-substitution is also associated with mixed valence states for Ni and Rh, where Ni(II)/Rh(IV) dominates for high Rh-contents ($x \geq 0.60$). The structural distortions of the phase transformation also result in a compositionally driven metal-to-insulator transition for $0.10 < x_{MIT} < 0.30$, caused by the decrease in the *M*-O-*M* bond angle. The reduced amount of Ni atoms contributing to metallic conductivity also contributes to the MIT, however, the effect is low compared to LaNi$_{1-x}$Co$_x$O$_3$. On the metallic side of the MIT ($x \leq 0.10$), Rh-substitution introduces disorder, resulting in reduced metallicity and high resistivity compared to other metals. While for the compositions showing insulating behaviour ($x \geq 0.30$), conduction occurs by activated hopping. At temperature above approximately $80\,K$, Arrhenius-type and polaron-type thermally activated hopping occur, while variable range hopping occurs at temperatures below approximately $70\,K$. The system further shows a magnetic transition at low temperature ($T_m \approx 10$ K) into a mixed ferro- and antiferromagnetic state. With increasing Rh-content, a change from dominating antiferro- to ferromagnetic interactions occurs, with a maximum at $x = 0.80$ and $x = 0.90$. This occurs due to mixed valence states for the different compounds, where Ni(III)/Rh(III) result in antiferromagnetism, while

11

Ni(II)/Rh(IV) lead to mixed ferro- and antiferromagnetism. The ferromagnetism is believed to originate from the Ni(II)-O-Rh(IV) super-exchange interactions, or related phenomena due to mixed oxidation states, and we believe that new ferromagnetic compounds with Ni(II)/Rh(IV) may exist.
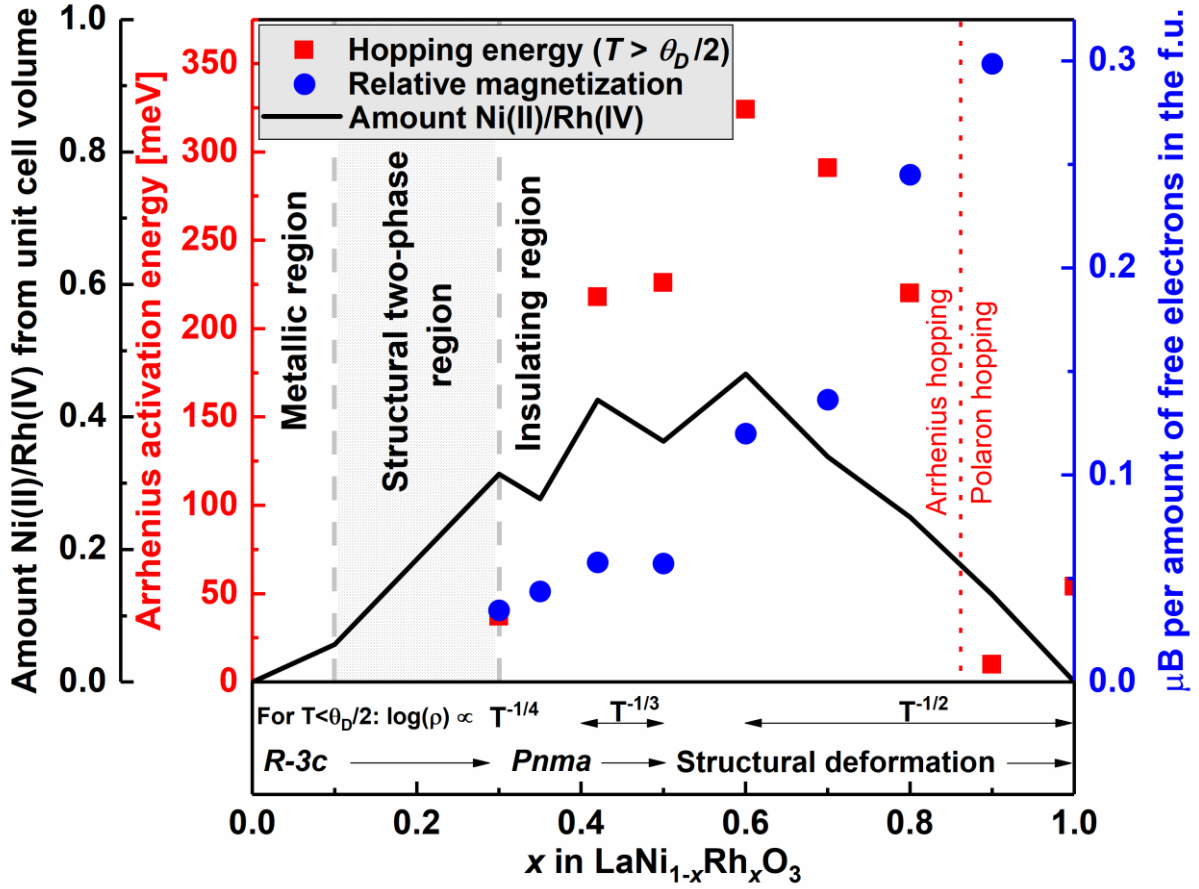

Figure 6. Summary of structural and electronic properties in the LaNi$_{1-x}$Rh$_x$O$_3$ system as function of Rh-content (x). It displays the amount of Ni(II) and Rh(IV) scaled to 1 from the change in slope in the unit cell volume (solid black line with left black axis), the development of the activation energy of the resistivity (red dots and left red axis) and the saturation magnetization [μ_B] relative to the amount of free electrons available on Ni(II), Ni(III) and Rh(IV) (blue points and right blue axis). The metallic region is indicated on the left, and the structural two-phase region with a grey area. The change from Arrhenius-type to polaron-type hopping is indicated with the red dotted line. The temperature dependency of the resistivity is shown near the bottom of the figure, and the space group and increased structural deformations are indicated at the bottom of the figure.

Acknowledgements

References

1.   Li, B., Louca, D., Yano, S., Marshall, L.G., Zhou, J., and Goodenough, J.B., *Insulating Pockets in Metallic LaNiO₃.* Advanced Electronic Materials, 2016. **2**(2): p. 1500261.

2. Zhou, J.S., Goodenough, J.B., and Dabrowski, B., *Exchange Interaction in the Insulating Phase of $RNiO_3$.* Physical Review Letters, 2005. **95**(12): p. 127204.

3. Zhou, J.S. and Goodenough, J.B., *Chemical bonding and electronic structure of $RNiO_3$, R= rare earth.* Physical Review B, 2004. **69**(15): p. 153105.

4. Kumar, S., Fjellvåg, Ø., Sjåstad, A.O., and Fjellvåg, H., *Physical properties of Ruddlesden-Popper (n = 3) nickelate: $La_4Ni_3O_{10}$.* Journal of Magnetism and Magnetic Materials, 2020. **496**: p. 165915.

5. Periyasamya, M., Patrab, L., Fjellvåg, Ø.S., Ravindranb, P., Magnus, H.S., Susmit, K., Sjåstad, A.O., and Fjellvåg, H., *Electron doping of $La_4Ni_3O_{10}$ by aluminium substitution.* *submitted, 2020.

6. Rajeev, K. and Raychaudhuri, A., *Quantum corrections to the conductivity in a perovskite oxide - a low-temperature study of $LaNi_{1-x}Co_xO_3$ ($0 \leq x \leq 0.75$).* Physical Review B, 1992. **46**(3): p. 1309-1320.

7. Rajeev, K.P., Shivashankar, G.V., and Raychaudhuri, A.K., *Low-temperature electronic properties of a normal conducting perovskite oxide ($LaNiO_3$).* Solid State Communications, 1991. **79**(7): p. 591-595.

8. Zhou, J.S., Marshall, L.G., and Goodenough, J.B., *Mass enhancement versus Stoner enhancement in strongly correlated metallic perovskites: $LaNiO_3$ and $LaCuO_3$.* Physical Review B, 2014. **89**(24): p. 245138.

9. Li, D., Lee, K., Wang, B.Y., Osada, M., Crossley, S., Lee, H.R., Cui, Y., Hikita, Y., and Hwang, H.Y., *Superconductivity in an infinite-layer nickelate.* Nature, 2019. **572**(7771): p. 624-627.

10. Vasala, S. and Karppinen, M., *$A_2B'B''O_6$ perovskites: A review.* Progress in Solid State Chemistry, 2015. **43**(1-2): p. 1-36.

11. Meneghini, C., Ray, S., Liscio, F., Bardelli, F., Mobilio, S., and Sarma, D.D., *Nature of ``Disorder'' in the Ordered Double Perovskite Sr_2FeMoO_6.* Physical Review Letters, 2009. **103**(4): p. 046403.

12. Sarma, D.D., Ray, S., Tanaka, K., Kobayashi, M., Fujimori, A., Sanyal, P., Krishnamurthy, H.R., and Dasgupta, C., *Intergranular Magnetoresistance in Sr_2FeMoO_6 from a Magnetic Tunnel Barrier Mechanism across Grain Boundaries.* Physical Review Letters, 2007. **98**(15): p. 157205.

13. Guo, H., Li, Z.W., Zhao, L., Hu, Z., Chang, C.F., Kuo, C.Y., Schmidt, W., Piovano, A., Pi, T.W., Sobolev, O., Khomskii, D.I., Tjeng, L.H., and Komarek, A.C., *Antiferromagnetic correlations in the metallic strongly correlated transition metal oxide $LaNiO_3$.* Nature Communications, 2018. **9**(1): p. 43.

14. Dey, K., Hergett, W., Telang, P., Abdel-Hafiez, M.M., and Klingeler, R., *Magnetic properties of high-pressure optical floating-zone grown $LaNiO_3$ single crystals.* Journal of Crystal Growth, 2019. **524**: p. 125157.

15. Garcia-Munoz, J.L., Rodriguez-Carvajal, J., Lacorre, P., and Torrance, J.B., *Neutron-diffraction study of $RNiO_3$ (R = La, Pr, Nd, Sm): electronically induced structural changes across the metal-insulator transition.* Phys. Rev. B: Condens. Matter, 1992. **46**(8): p. 4414-25.

16. Lacorre, P., Torrance, J.B., Pannetier, J., Nazzal, A.I., Wang, P.W., and Huang, T.C., *Synthesis, crystal structure, and properties of metallic praseodymium nickel oxide ($PrNiO_3$): comparison with metallic neodymium nickel oxide ($NdNiO_3$) and semiconducting samarium nickel oxide ($SmNiO_3$).* J. Solid State Chem., 1991. **91**(2): p. 225-37.

17. Alonso, J.A., Martínez-Lope, M.J., Casais, M.T., García-Muñoz, J.L., Fernández-Díaz, M.T., and Aranda, M.A.G., *High-temperature structural evolution of $RNiO_3$ (R = Ho, Y, Er, Lu) perovskites: Charge disproportionation and electronic localization.* Physical Review B, 2001. **64**(9): p. 094102.

18. Androulakis, J., Viskadourakis, Z., Katsarakis, N., and Giapintzakis, J., *Magnetoresistance and percolation in the $LaNi_{1-x}Co_xO_3$ solid solution.* 2003.

19. Alonso, J.A., García-Muñoz, J.L., Fernández-Díaz, M.T., Aranda, M.A.G., Martínez-Lope, M.J., and Casais, M.T., *Charge Disproportionation in $RNiO_3$ Perovskites: Simultaneous Metal-Insulator and Structural Transition in $YNiO_3$.* Physical Review Letters, 1999. **82**(19): p. 3871-3874.

20. Vasanthacharya, N.Y., Ganguly, P., Goodenough, J.B., and Rao, C.N.R., *Valence states and magnetic properties of LaNi$_{1-x}$Mn$_x$O$_3$ (for $0 \leqslant x \leqslant 0.2$ and $x = 0.5$).* Journal of Physics C: Solid State Physics, 1984. **17**(15): p. 2745-2760.

21. Asai, K., Sekizawa, H., Mizushima, K., and Iida, S., *Magnetic Properties of LaNi$_{1-x}$Co$_x$O$_3$ ($0 \leq x \leq 0.5$).* Journal of the Physical Society of Japan, 1977. **43**(3): p. 1093-1094.

22. Asai, K., Sekizawa, H., Mizushima, K., and Iida, S., *Magnetic Properties of LaNi$_{1-x}$Fe$_x$O$_3$ ($0 \leq x \leq 0.2$).* Journal of the Physical Society of Japan, 1978. **45**(4): p. 1417-1418.

23. Schinzer, C., *Spin-glass behavior of disordered perovskite LaNi$_{1/2}$Rh$_{1/2}$O$_3$.* J. Alloys Compd., 1999. **288**(1-2): p. 65-75.

24. Battle, P.D. and Vente, J.F., *Structural and Magnetic Characterization of La$_2$NiRhO$_6$.* J. Solid State Chem., 1999. **146**(1): p. 163-167.

25. Rao, C.N.R., Parkash, O.M., and Ganguly, P., *Electronic and magnetic properties of LaNi$_{1-x}$Co$_x$O$_3$, LaCo$_{1-x}$Fe$_x$O$_3$ and LaNi$_{1-x}$Fe$_x$O$_3$.* Journal of Solid State Chemistry, 1975. **15**(2): p. 186-192.

26. Goodenough, J.B., *Magnetism and the chemical bond.* Interscience monographs on chemistry, Inorganic chemistry section. Vol. vol. 1. 1963, New York: Interscience.

27. Smith, A.E., Sleight, A.W., and Subramanian, M.A., *Electrical and magnetic properties of new rhodium perovskites: La2MRhO6, M=Cr, Fe, Cu.* Mater. Res. Bull., 2010. **45**(4): p. 460-463.

28. Yamaura, K., Huang, Q., Young, D.P., Noguchi, Y., and Takayama-Muromachi, E., *Crystal structure and electronic and magnetic properties of the bilayered rhodium oxide Sr$_3$Rh$_2$O$_7$.* Physical Review B, 2002. **66**(13): p. 134431.

29. Perry, R.S., Baumberger, F., Balicas, L., Kikugawa, N., Ingle, N.J.C., Rost, A., Mercure, J.F., Maeno, Y., Shen, Z.X., and Mackenzie, A.P., *Sr$_2$RhO$_4$: a new, clean correlated electron metal.* New Journal of Physics, 2006. **8**(9): p. 175-175.

30. Yamaura, K. and Takayama-Muromachi, E., *Enhanced paramagnetism of the 4d itinerant electrons in the rhodium oxide perovskite SrRhO$_3$.* Physical Review B - Condensed Matter and Materials Physics, 2001. **64**(22): p. 2244241-2244245.

31. van Beek, W., Safonova, O.V., Wiker, G., and Emerich, H., *SNBL, a dedicated beamline for combined in situ X-ray diffraction, X-ray absorption and Raman scattering experiments.* Phase Transitions, 2011. **84**(8): p. 726-732.

32. Coelho, A.A., *TOPAS and TOPAS-Academic: an optimization program integrating computer algebra and crystallographic objects written in C++.* Journal of Applied Crystallography, 2018. **51**(1): p. 210-218.

33. Kojima, T., Nomura, K., Miyazaki, Y., and Tanimoto, K., *Synthesis of Various LaMO$_3$ Perovskites in Molten Carbonates.* Journal of the American Ceramic Society, 2006. **89**(12): p. 3610-3616.

34. Ravel, B. and Newville, M., *ATHENA, ARTEMIS, HEPHAESTUS: data analysis for X-ray absorption spectroscopy using IFEFFIT.* J Synchrotron Radiat, 2005. **12**(Pt 4): p. 537-41.

35. Barton, P.T., Seshadri, R., and Rosseinsky, M.J., *Electrical and magnetic properties of the complete solid solution series between SrRuO$_3$ and LaRhO$_3$: Filling t2g versus tilting.* Phys. Rev. B: Condens. Matter Mater. Phys., 2011. **83**(6): p. 064417/1-064417/8.

36. Glazer, A.M., *The classification of tilted octahedra in perovskites.* Acta Crystallographica Section B, 1972. **28**(11): p. 3384-3392.

37. Li, J., Smith, A.E., Kwong, K.-S., Powell, C., Sleight, A.W., and Subramanian, M.A., *Lattice crossover and mixed valency in the LaCo$_{1-x}$Rh$_x$O$_3$ solid solution.* Journal of Solid State Chemistry, 2010. **183**(6): p. 1388-1393.

38. Rodríguez-Carvajal, J., Hennion, M., Moussa, F., Moudden, A.H., Pinsard, L., and Revcolevschi, A., *Neutron-diffraction study of the Jahn-Teller transition in stoichiometric LaMnO$_3$.* Physical Review B, 1998. **57**(6): p. R3189-R3192.

39. Vegard, L., *Die Konstitution der Mischkristalle und die Raumfüllung der Atome.* Zeitschrift für Physik, 1921. **5**(1): p. 17-26.

40. Shannon, R.D., *Revised effective ionic radii and systematic studies of interatomic distances in halides and chalcogenides.* Acta Crystallographica Section A, 1976. **32**(5): p. 751-767.

41. Shibasaki, S., Takahashi, Y., and Terasaki, I., *Thermoelectric properties of LaRh$_{1-x}$Ni$_x$O$_3$.* J. Phys.: Condens. Matter, 2009. **21**(11): p. 115501/1-115501/4.

42. Kagan, Y. and Flerov, V.N., *Theory of the resistivity and magnetoresistance of metals at low temperatures.* Journal of Experimental and Theoretical Physics, 1974. **66**(4): p. 1374-1386.

43. Chainani, A., Sarma, D.D., Das, I., and Sampathkumaran, E.V., *Low-temperature electrical conductivity of LaNi$_{1-x}$Fe$_x$O$_3$.* Journal of Physics: Condensed Matter, 1996. **8**(43): p. L631-L636.

44. Chaitanya Lekshmi, I., Gayen, A., and Hegde, M.S., *Electrical transport properties of LaNi$_{1-x}$M$_x$O$_3$ (M = Co, Mn) thin films fabricated by pulsed laser deposition.* Journal of Physics: Condensed Matter, 2005. **17**(41): p. 6445-6458.

45. Niwa, E., Uematsu, C., Miyashita, E., Ohzeki, T., and Hashimoto, T., *Conductivity and sintering property of LaNi$_{1-x}$Fe$_x$O$_3$ ceramics prepared by Pechini method.* Solid State Ionics, 2011. **201**(1): p. 87-93.

46. Austin, I.G. and Mott, N.F., *Polarons in crystalline and non-crystalline materials.* Advances in Physics, 2001. **50**(7): p. 757-812.

47. Varshney, D. and Dodiya, N., *Metallic and semi-conducting resistivity behaviour of La$_{0.7}$Ca$_{0.3-x}$K$_x$MnO$_3$ (x = 0.05, 0.1) manganites.* Journal of Theoretical and Applied Physics, 2015. **9**(1): p. 45-58.

48. Mott, N.F., *Electronic processes in non-crystalline materials*. 2nd ed. ed. The International series of monographs on physics, ed. Davis, E.A. 1979, Oxford: Clarendon Press.

49. Mott, N.F., *Conduction in glasses containing transition metal ions.* Journal of Non-Crystalline Solids, 1968. **1**(1): p. 1-17.

50. Efros, A.L. and Shklovskii, B.I., *Coulomb gap and low temperature conductivity of disordered systems.* Journal of Physics C: Solid State Physics, 1975. **8**(4): p. L49-L51.

51. Tilley, R.J.D., *Understanding solids : the science of materials*. 2nd ed. ed. 2013, Chichester: Wiley.

52. Bałanda, M., *AC susceptibility studies of phase transitions and magnetic relaxation: Conventional, molecular and low-dimensional magnets*. 2013. p. 964-976.

53. Anand, V.K., Adroja, D.T., Hillier, A.D., and Anand, A.D., *Ferromagnetic cluster spin-glass behavior in PrRhSn$_3$.* Physical Review B - Condensed Matter and Materials Physics, 2012. **85**(1).